Col6 deficiency in a zebrafish model of Bethlem myopathy leads to dysfunction of the muscle dihydropyridine receptor

Romane Idoux[1], Chloé Exbrayat-Heritier[2], Shivashakthi Shivaraman[2], Francisco Jaque-Fernandez[1], Adrien Ducret[3], Christine Berthier[1], Vincent Jacquemond[1], Frédéric Sohm[2], Sandrine Bretaud[2], Florence Ruggiero[2]* and Bruno Allard[1]*

[1]Pathophysiology and Genetics of Neuron and Muscle – Lyon (France)

[2]Institut de Génomique Fonctionnelle de Lyon – Lyon (France)

[3]Molecular Microbiology and Structural Biochemistry – Lyon (France)

*co-corresponding authors and equally contributed to the work

Abstract:
Bethlem myopathy (BM) is an incurable muscle disease characterized by joint contractures and muscle weakness worsening with age. BM results from mutations in genes encoding one of the three α chains of collagen VI (ColVI), a component of the skeletal muscle extracellular matrix produced by interstitial fibroblasts. A still unresolved issue in BM is how alteration in ColVI present outside muscle fibers induces dysfunction within muscle fibers. In the present study, we explored properties of excitation-contraction coupling on isolated fast skeletal muscle fibers from one-year old zebrafish *col6a1*$^{\Delta ex14}$ harboring an exon-skipping mutation (*col6a1*$^{\Delta ex14}$) that is the most frequently found in BM patients. *Col6a1*$^{\Delta ex14}$ fish muscle exhibited age-dependent progressive loss of ColVI deposition, accompanied with defects in basement membrane organization and ColVI intracellular accumulation. Muscle action potentials were found to be unchanged in *col6a1*$^{\Delta ex14}$ fish as compared to wild-type. The density of charge movements produced by depolarization-induced activation of dihydropyridine receptors (DHPRs), that control sarcoplasmic reticulum (SR) Ca^{2+} release, was found to be reduced and their voltage-dependence shifted toward negative potentials in *col6a1*$^{\Delta ex14}$ fish. Concomitantly, the voltage dependence of depolarization-evoked intracellular Ca^{2+} transients was also shifted toward negative voltages, promoting in this way an elevated pathogenic SR Ca^{2+} leak at resting membrane potentials, as evidenced by higher density of Ca^{2+} sparks at rest, larger SR Ca^{2+} release in response to long-duration depolarizations between -70 and -40 mV and reduced twitch muscle force and swimming performance. Finally, clusters of α1S subunits of DHPR were found to be mis-localized in mutant fibers t-tubules. These data suggest that Col6 deficiency in BM leads to an alteration of the DHPR function that contributes to promote a pathogenic SR Ca^{2+} leak. DHPR could represent the still elusive link that allows altered myomatrix to transduce pathogenic signals within muscle.

Introduction

Bethlem myopathy (BM) is a debilitating genetic disorder characterized by abnormal contractures of the Achilles tendons, elbows, shoulders, spine and finger flexors, experienced as joint stiffness and associated with proximal muscle weakness. Progressive muscle wasting also occurs and symptoms worsen in the 4th and 5th decades of life with increasing risk of respiratory insufficiency and ambulation difficulties (Bönnemann, 2011; Lampe, 2005; Lamandé and Bateman, 2018). The pathology is incurable and its prevalence is 0.77 per 100,000. BM is an autosomal dominant disease caused by mutations in the COL6A1, COL6A2, COL6A3 genes that encode the three major chains of collagen type VI (ColVI)-, α1, α2, α3 respectively. ColVI is a component of the extracellular matrix (ECM) with a broad tissue distribution including high expression in skeletal muscle. In skeletal muscle, ColVI is produced by interstitial fibroblasts where three ColVI α-chains assemble into triple-helix monomers, themselves assembling into dimers, then tetramers that are secreted in the extracellular space to associate into characteristic beaded microfilaments (Colombatti et al., 1995; Cescon et al., 2015). ColVI binds to a large number of ECM components, structuring in this way the three-dimensional architecture of the tissue and connecting directly or indirectly muscle cells to ECM (Cescon et al., 2015). Nowadays, a still unresolved issue is to understand how a disrupted ColVI protein belonging to ECM can induce pathologic muscle dysfunction?

In an attempt to address this question, some animal models were generated such as a mouse and a zebrafish model in which the *col6a1* gene has been invalidated (Bonaldo, 1998; Toneletto et al., 2022). Expression of different Col6 α chains has been also transitory knocked down by morpholinos injection in zebrafish larvae (Telfer et al., 2010). Among these models, several muscle abnormalities have been reported such as a loss of contractile strength, sarcoplasmic reticulum (SR) alterations, neuromuscular transmission deficiency and structural and functional impairment of mitochondria (Irwin et al., 2003; Cescon et al., 2018; Telfer et al., 2010; Toneletto et al., 2022). However, microinjection of morpholinos in developing embryos provokes transient knockdown of targeted genes while BM is a progressive disease. Moreover, invalidation of *col6a1* gene in *col6a1*$^{-/-}$ mice provokes a complete loss of ColVI expression, while BM in human results from mutations in one of the three ColVI α chains.

In order to circumvent these limitations, Radev et al. (2015) created the first zebrafish line harboring a mutation that is the most frequently found in BM patients. Using a transcription activator-like effector nuclease (TALEN) strategy, they provoked a deletion in a splice donor site leading to an in-frame skipping of exon 14 in *col6a1* mRNA (*col6a1*$^{\Delta ex14}$). As described in *col6a1*$^{-/-}$ mouse and morpholino-knock down zebrafish models, ultrastructural analysis of zebrafish *col6a1*$^{\Delta ex14}$ trunks at 6-7 dpf, 1 week and 1 year revealed the same ultrastructural abnormalities, including SR alteration, which worsen with age as observed in the human disease (Radev et al., 2015).

Interestingly, it was found that intracellular Ca^{2+} increase provoked by inhibition of the mitochondrial F_1/F_0 ATPase was larger and occurred earlier in muscle from *col6a1*$^{-/-}$ as compared to wild-type (WT) mice and was suppressed by dantrolene, a blocker of SR Ca^{2+} release channel (Irwin et al., 2003), suggesting a possible dysfunction of SR Ca^{2+} flux associated with SR structure alterations as observed in mice and in *col6a1*$^{\Delta ex14}$ zebrafish. In skeletal muscle, Ca^{2+} ions activating contraction are released by the SR in response to muscle excitation through the excitation-contraction (EC) coupling process. During this process, action potentials activate the dihydropyridine receptor (DHPR), resulting in intramembrane charge movements, which in turn opens the ryanodine receptor (RyR_1), a Ca^{2+} release channel anchored in the SR membrane (Allard, 2018). We recently provided a comprehensive characterization of EC coupling properties of isolated fast muscle fibers from adult zebrafish and demonstrated that zebrafish EC coupling displays superfast properties (Idoux et al., 2022). The reported effect of dantrolene and altered SR structure in *col6a1* deficient muscle fibers, together with the fact that BM symptoms worsen with age, prompted us to explore in the present study the properties of EC coupling using current- and voltage-clamp combined with intracellular Ca^{2+} measurement in isolated fibers from *col6a1*$^{\Delta ex14}$ zebrafish at adult stage. Additionally, we characterized the defects in synthesis, secretion, oligomerization and expression of Col6 α1 chains in muscles from adult *col6a1*$^{\Delta ex14}$ zebrafish. Our data give evidence of an alteration of the functional expression and of

the voltage-dependence of the DHPR that contributes to promote a pathogenic SR Ca^{2+} leak in *col6a1*$^{\Delta ex14}$ zebrafish.

Results

Loss of ColVI deposition is accompanied with defects in basement membrane and ColVI intracellular accumulation in *col6a1*$^{\Delta ex14}$ zebrafish muscle

The exon 14 deletion in ***col6a1*** predicts a truncated collagen VI α1 chain (Ravel et al., 2015), which may interfere with trimer formation alongside its two partner chains, α2(VI) and α3(VI). To assess trimer assembly and secretion of collagen VI, we performed immunofluorescence staining using guinea pig antibodies raised against the recombinant C-terminal domain of the zebrafish α1(VI) chain (see Materials and Methods) on frozen muscle sections from 6-month-old and 1-year-old mutant and wild-type (WT) zebrafish (Fig. 1).

In WT fish, a continuous ColVI staining outlining all muscle fibers is observed (Fig. 1A). In striking contrast, ***col6a1***$^{\Delta ex14}$ mutants show an interrupted, patchy collagen VI signal surrounding muscle cells. This suggests that the production of the truncated α1(VI) chain by muscle fibroblasts impairs the extracellular ColVI filament assembly. Intriguingly, ColVI immunoreactivity is nearly absent in 1-year-old wild-type muscle, mirroring the age-related decline in BM patients.

ColVI is a basement membrane-associated collagen (Cescon et al., 2015). We therefore examined whether disorganized ColVI or its age-dependent loss in 1-year-old muscle affects laminin deposition, a major basement membrane component. Immunofluorescence using pan-laminin antibodies revealed that laminin deposition is disrupted in mutant muscle, presenting as a patchy pattern at both 6 months and 1 year (Fig. 1A). Unlike ColVI, laminin remains detectable with age, although its organization was clearly disturbed.

ColVI immunoreactivity was further confirmed on isolated muscle cells from zebrafish trunks (Fig. 1B). This allowed the observation of an intracellular retention of ColVI in neighboring fibroblasts, the primary source of ColVI in skeletal muscle, indicating that although these cells still produce the mutant protein, its secretion is impaired.

Due to ColVI insolubility, its extraction from skeletal muscle is challenging, we thus performed Western blot analysis on protein extracts from the skin, where ColVI is abundantly expressed by dermal fibroblasts. Results revealed the almost absence of the α1(VI) chain band in mutant samples, in contrast to wild-type skin, confirming impaired collagen VI deposition in BM fish (Fig. 1C).

In conclusion, ColVI deposition is disrupted in the ***col6a1***$^{\Delta ex14}$ mutant fish, characterized by at best a patchy presence of the protein around skeletal muscle fibers. This disruption affects basement membrane assembly and may impair its mechanical and/or signaling roles in mutant skeletal muscle.

T-tubule structure is not altered in *col6a1*$^{\Delta ex14}$ zebrafish muscle fibers

In skeletal muscle, excitation-contraction coupling involves two membrane systems, the transverse tubules and the SR. The T tubules correspond to extensions of the sarcolemma that penetrate into the depth of the fiber to permit action potentials propagation. In order to explore possible alterations in the structure of t-tubules, isolated WT and *col6a1*$^{\Delta ex14}$ muscle fibers were stained with di-8-anepps. Fig 2A shows confocal images of di-8-anepps fluorescence in a WT fiber (left) and a *col6a1*$^{\Delta ex14}$ fiber (right). In both fiber populations, the fluorescence patterns were comparable and showed transverse striations characteristic of t-tubule localization at the level of Z-lines of the sarcomere in zebrafish muscle. The distance between two peaks of di-8anepps fluorescence, corresponding to t-tubules interval as well as sarcomere length, were found to be not significantly different in WT (1.84 ± 0.006 µm) and *col6a1*$^{\Delta ex14}$ fibers (1.85 ± 0.014 µm) (Fig. 2B, C). In addition, no sign of misorientation of the t-tubule network was observed in the *col6a1*$^{\Delta ex14}$ group and t-tubule density was not significantly different in the two groups (Fig. 2C). These data reveal that the t-tubule network is not impaired in *col6a1*$^{\Delta ex14}$ zebrafish.

Action potentials properties are not affected in *col6a1$^{\Delta ex14}$* zebrafish muscle fibers

Under physiological conditions, the first step of EC coupling corresponds to the firing and propagation of action potential along sarcolemma and t-tubules. A series of current-clamp experiments were performed to measure action potentials in WT and *col6a1$^{\Delta ex14}$* fibers. In both fiber populations, injection of 0.5-ms duration suprathreshold depolarizing current from a resting membrane potential held at -110 mV and in the presence of an external Tyrode solution induced action potentials (Fig. 3A). In WT muscle, as described previously, the peak value of voltage reached by action potentials was close to 0 mV and the repolarization phase displayed very fast kinetics (Idoux et al., 2022). Fig 3B shows that maximal amplitude, time to peak and time for 20, 50 and 80 % repolarization of action potential after spike were found to be not significantly different in WT and *col6a1$^{\Delta ex14}$* muscle fibers. These data suggest that membrane excitable properties are not affected in *col6a1$^{\Delta ex14}$* fish muscle.

Reduced maximal density and negative shift of voltage dependence of intramembrane charge movements in *col6α1$^{\Delta ex14}$* zebrafish muscle fibers

A next series of experiments aimed at studying the functionality of the DHPR that controls in a voltage-dependent manner the opening of RyR_1 channels, the SR Ca^{2+} channels responsible for the intracellular Ca^{2+} release. For this purpose, the membrane currents resulting from the movement of intramembrane charges carried by the α1S subunit of the DHPR were recorded in response to depolarization. Figure 4A shows currents produced by intramembrane charge movements recorded in a voltage-clamped zebrafish muscle fiber in the absence of external Na^+ and K^+ ions and in the presence of Na^+ and K^+ channel blockers and low Cl^- from a holding potential of -80 mV in WT and *col6α1$^{\Delta ex14}$* muscle fiber. The density of "on" charges (Q_{on}) was plotted as a function of voltage and the relationship was fitted in each cell with a Boltzmann equation (Fig. 4B, C). The mean values for Q_{max}, $V_{0.5}$, and k were 8.8 ± 0.7 nC/µF, −32.5 ± 1.5 mV, and 9 ± 0.4 mV for WT fish and 6.3 ± 0.7 nC/µF, -41.4 ± 1.4 mV, and 6.7 ± 0.4 mV for *col6a1$^{\Delta ex14}$* fish respectively (Fig. 4D). The maximal charges density (Q_{max}) was significantly reduced in *col6a1$^{\Delta ex14}$* fibers indicating a lower density of functional DHPR in *col6a1$^{\Delta ex14}$* fish (P= 0.027). The voltage dependence of charge movements was also significantly steeper (P= 0.033) and shifted toward negative potentials in *col6a1$^{\Delta ex14}$* fish (P= 0.018).

The voltage dependence of SR Ca^{2+} release is also shifted toward negative potentials in *col6α1$^{\Delta ex14}$* zebrafish muscle fibers

By activating DHPR proteins, depolarization induces the opening of SR Ca^{2+} release channels. Using the same external solution as the one used for recording charge movements, intracellular Ca^{2+} transients were measured in response to 50-ms duration depolarizing pulses of increasing amplitudes with the ratiometric Ca^{2+} indicator indo-1 dialyzed into WT and *col6a1$^{\Delta ex14}$* cells (Fig 5A). The indo-1 % saturation was plotted as a function of voltage and the relationship was fitted in each cell with a Boltzmann equation (Fig. 5B). Values for maximal indo-1 % saturation, $V_{0.5}$, and k were 53.2 ± 2.6 %, -30.6 ± 0.8 mV and 7.2 ± 0.2 mV for WT fish and 55.6 ± 2.4 %, -35.8 ± 0.9 mV and 7.2 ± 0.3 mV for *col6a1$^{\Delta ex14}$* fish respectively. Maximal amplitude of voltage-induced Ca^{2+} transients and steepness of voltage-dependence were not significantly changed in *col6a1$^{\Delta ex14}$* fibers but the voltage dependence was significantly shifted toward negative potentials (P = 0.007). The mean indo-1 % saturation in fibers held at -80 mV was found to be not significantly changed in *col6a1$^{\Delta ex14}$* fibers.

We showed in a previous study that prolongation of depolarization induces a progressive decline of the amplitude of Ca^{2+} transients resulting from a time- and voltage-dependent inactivation of DHPR (Idoux et al., 2022). This inactivation process was investigated in WT and *col6a1$^{\Delta ex14}$* by applying 50-ms duration voltage pulses to 0 mV from holding potentials incrementally depolarized during 20 s (Fig 6A). The relative amplitude of the Ca^{2+} transients was plotted as a function of the holding potential in each cell and the relationships were fitted with a Boltzmann equation (Fig. 6B). Values for $V_{0.5}$ and k were -67.7 ± 3.4 mV and 8.2 ± 0.7 mV for WT fish and -59.6 ± 2.7 mV and 6.7 ± 0.6 mV for *col6a1$^{\Delta ex14}$* fish respectively. Although the relationship between Ca^{2+} release inactivation and voltage in *col6a1$^{\Delta ex14}$* fish tended to be shifted toward positive potentials, none of these parameters were significantly different.

Intracellular Ca^{2+} changes are more elevated in response to long duration pulses of low amplitude in *col6a1$^{\Delta ex14}$* zebrafish muscle fibers

The negative shift of the voltage activation of charge movements and SR Ca^{2+} release observed in *col6a1$^{\Delta ex14}$* fiber suggest that opening of RyR_1 may occur at membrane potentials more negative than the voltage threshold of Ca^{2+} release usually observed between -50 and -40 mV in WT muscle (Idoux et al., 2022). The use of 50-ms duration depolarizing pulses together with global fluorescence measurements in the preceding experiments did not provide the required resolution for exploring intracellular Ca^{2+} changes provoked by low values of depolarization. Hence, in order to assess possible changes in voltage sensitivity of the DHPR at membrane potentials more negative than -50 mV, we measured intracellular Ca^{2+} changes in response to 10-s depolarizing pulses from a holding potential of -90 mV using Fluo-4 fluorescence confocal imaging in WT and *col6a1$^{\Delta ex14}$* fibers. Figure 7A shows that Ca^{2+} changes induced by depolarizing pulses from -80 to -60 mV were significantly larger in the *col6a1$^{\Delta ex14}$* fiber. In average, plotting the changes in fluorescence as a function of depolarization indicated that the maximal Ca^{2+} level reached during the pulses was significantly higher for all depolarization pulses from -80 to -60 mV in *col6a1$^{\Delta ex14}$* (Fig. 7B). In addition, it can be observed in Fig. 7A that Ca^{2+} remained at a larger level between pulses in the *col6a1$^{\Delta ex14}$* fiber. In average, plotting the changes in the basal fluorescence before each pulse as a function of depolarization showed that the basal Ca^{2+} increased at a significantly higher level with consecutive pulses in *col6a1$^{\Delta ex14}$* fibers.

Higher Ca^{2+} sparks occurrence in resting conditions in *col6a1$^{\Delta ex14}$* zebrafish muscle fibers

The shifted activation of SR Ca^{2+} release toward negative voltages might suggest that the active control of DHPR on gating of RyR_1 channel demonstrated in resting skeletal muscle (Robin and Allard, 2012) is impaired in *col6a1$^{\Delta ex14}$* fibers, leading to elevated SR Ca^{2+} efflux at rest. Elevated SR Ca^{2+} efflux induced by a loss of DHPR repressive action on RyR_1 channel is known to be correlated with an increase in the occurrence of spontaneous elementary events of SR Ca^{2+} release, named Ca^{2+} sparks (Ríos, 2018). We thus looked to such events in WT and *col6a1$^{\Delta ex14}$* fibers loaded with Fluo4. Figure 8A shows fluorescence images of a WT and a *col6a1$^{\Delta ex14}$* fiber in which Ca^{2+} ions were homogeneously distributed in the cytosol. No Ca^{2+} sparks were detected in the WT fiber while three Ca^{2+} sparks were detected at the same time in the *col6a1$^{\Delta ex14}$* fiber. Quantification of the percentage of fiber area exhibiting Ca^{2+} sparks in each fiber indicated that, in average, this relative fiber area was significantly larger in *col6a1$^{\Delta ex14}$* fibers (Fig. 8B). However, because a strong variability of Ca^{2+} sparks occurrence was observed from cell to cell, we classified WT and *col6a1$^{\Delta ex14}$* fibers according to different ranges of active area (Fig. 8C). Comparable numbers of WT and *col6a1$^{\Delta ex14}$* fibers were found to display any or very low active area but 4 *col6a1$^{\Delta ex14}$* fibers and none of WT fibers displayed Ca^{2+} sparks with a relative active area between 0.4 and 1%.

Alteration of DHPR distribution along t-tubules in *col6a1$^{\Delta ex14}$* zebrafish muscle fibers

The observed changes in density of charge movements, SR Ca^{2+} release and Ca^{2+} sparks in mutant fish point out to a dysfunction of DHPR resulting from Col6 deficiency. These data prompted us to explore the expression pattern of DHPR proteins using immunofluorescence labelling with antibodies raised against the α1s subunit of DHPR in WT and in *col6a1$^{\Delta ex14}$* fibers. Fluorescent confocal images revealed in both fish an intracellular striated expression pattern consistent with location of DHPR in t-tubules (Fig. 9A). Spacing between fluorescent striations were found to be not significantly different in WT and in *col6a1$^{\Delta ex14}$* fibers, confirming that t-tubule periodicity and sarcomere length were not altered in mutant fish. As already described in myotubes from zebrafish larvae (Schredelseker *et al.*, 2005), transverse striations consisted in alignments of fluorescent foci corresponding to clusters of α1S at the level of t-tubule/SR junctions. The mean distance between foci was found to be very significantly shorter in mutant fish (Fig. 9B).

Twitch muscle force and swimming performance are lower in *col6a1$^{\Delta ex14}$* zebrafish

A last series of experiments were performed in order to determine whether the observed changes in EC coupling in *col6a1$^{\Delta ex14}$* muscle were associated with a change in muscle performance under

physiological conditions. To address this question, we first measured force developed by trunk muscle from 2 wpf WT and mutant fish in response to electrical field stimulation. Figure 10A and 10B show that the contractile force generated by mutant muscles was lower than WT and the mean amplitude of the twitch response was about one third smaller than WT. Swimming performance was also measured in one-year old WT and *col6a1*$^{\Delta ex14}$ zebrafish. Fish were placed in a swim tunnel and challenged by increasing water flows against which fish managed to swim (Fig. 10C). Figure 10D shows that the maximal velocity fish could reach during a swimming step protocol expressed as U_{crit} was significantly lower in *col6a1*$^{\Delta ex14}$ as compared to WT zebrafish (6.99 ± 0.37 BL.s^{-1} for WT vs 8.87 ± 0.52 BL.s^{-1} for *col6a1*$^{\Delta ex14}$; P = 0.0073).

Discussion

The main finding of our study is that the *col6a1*$^{\Delta ex14}$ mutation responsible for BM in human induces a reduced expression of functional DHPR and a negative shift of its voltage dependence contributing to an elevated SR Ca^{2+} leak at negative potentials. Throughout this study, we explored all the steps of EC coupling, from excitation to SR Ca^{2+} release. We first showed that amplitude and kinetics of action potential were not altered by the mutation, indicating that properties of ion channels involved in the firing of action potential were not modified. In contrast, density and voltage sensitivity of the second step of EC coupling, corresponding to the activation of DHPR and resulting in charge movements, were found to be reduced and shifted by 9 mV towards negative membrane potentials respectively. DHPR proteins are mainly anchored in the t-tubule membranes and it might be hypothesized that the observed modifications could be due to a disorganization of this membrane system. However, confocal imaging of fibers stained with di-8anepps and antibodies raised against α1s subunit of DHPR showed that density and orientation of t-tubules were not altered in *col6a1*$^{\Delta ex14}$ fish. It is thus likely that Col6 deficiency specifically reduces expression of functional DHPR and disrupts its voltage sensitivity. Since DHPR controls in a voltage-dependent manner the opening of the SR Ca^{2+} release channel, it was predictable that the maximal capacity and the voltage-dependence of SR Ca^{2+} release would also be reduced and shifted toward negative voltages respectively. We however did not find any significant change in the maximal amplitude of voltage-activated Ca^{2+} transients and measured a shift of only 5 mV of the voltage-dependence, about half of the shift of charge movements, without any change in the inactivation process. In a recent paper, we reported a reduced intramembrane charge movements density in zebrafish muscle as compared to mammalian muscle but likely compensated by a higher efficacy of coupling between DHPR and SR Ca^{2+} release channel since the maximal amplitude of voltage-activated Ca^{2+} transients was found to be comparable to the one recorded in mammalian muscle (Idoux *et al*., 2022). It thus can be suggested that the changes in charge density and voltage-dependence of DHPR could be dampened following coupling with SR Ca^{2+} release because of this elevated coupling efficiency, explaining in this way the unchanged SR Ca^{2+} release capacity and the lesser voltage shift of SR Ca^{2+} release activation.

Under physiological conditions of activation of the muscle fiber, T-tubular depolarization induced by action potentials always maximally activates SR Ca^{2+} release. Since the maximal capacity of SR Ca^{2+} release was not changed in *col6a1*$^{\Delta ex14}$ fish muscle, we envisioned that the hyperpolarizing shift of activation of DHPR and of SR Ca^{2+} release should not greatly impact muscle function during activation. However, DHPR is known to exert an active control on the SR Ca^{2+} release channel over the whole voltage range from resting membrane potential values to values inducing maximal Ca^{2+} release (Robin and Allard, 2012). This led us to explore SR Ca^{2+} release capacity at voltages closer to resting membrane potentials that do not elicit detectable intracellular Ca^{2+} changes in response to short duration pulses. We showed that, in response to 10-s duration voltage pulses, the magnitude of Ca^{2+} release was larger for depolarizations from -80 to -60 mV in *col6a1*$^{\Delta ex14}$ fibers as compared to WT fibers. These data demonstrate that the shift of voltage-dependence of DHPR activation occurs in mutant fibers over the whole voltage range including membrane potentials close to resting values and may give rise to an elevated SR Ca^{2+} efflux at resting membrane potentials. Additionally, we observed that the basal Ca^{2+} remained at higher levels between voltage pulses in *col6a1*$^{\Delta ex14}$ fibers, possibly caused by an increased

SR Ca^{2+} efflux at -90 mV. Moreover, when we looked at Ca^{2+} sparks, we measured a significant higher relative area displaying Ca^{2+} sparks in *col6a1*$^{\Delta ex14}$ fibers, likely reflecting an elevated SR Ca^{2+} efflux in resting fibers. However, RyR_1 is not the only SR Ca^{2+} release channel present in zebrafish muscle. Another isoform, RyR_3, has indeed been shown to be localized in the parajunctional SR (Perni et al., 2015). Silencing RyR_3 by morpholino injection in zebrafish larvae was found to cause a dramatic reduction in Ca^{2+} sparks, suggesting that RyR3 is the main contributor to the SR Ca^{2+} flux underlying Ca^{2+} sparks (Perni et al., 2015). RyR_3 opening is considered to be not under the direct control of DHPR but activated by Ca^{2+} flowing through RyR1 *via* a Ca^{2+}-induced Ca^{2+} release process as proposed for frog muscle (Shirokova et al., 1998). In these conditions, the higher frequency of Ca^{2+} sparks that we observed cannot be directly the consequence of a shift of voltage-dependence of DHPR, but, indirectly, could result from a higher efflux of Ca^{2+} through RyR_1 due to this shift, which in turn over-activates RyR_3 channels *via* a Ca^{2+}-induced Ca^{2+} activation process.
Hence, our data lead us to propose that the BM mutation promotes an exacerbated resting SR Ca^{2+} efflux by disrupting the voltage-dependent DHPR-gated RyR_1 activity. An elevated resting SR Ca^{2+} efflux has been described in a number of muscle disorders (Bellinger et al., 2009; Robin et al., 2012). This elevated SR Ca^{2+} leak is thought to increase protein degradation, mitochondrial dysfunction, and dilated SR as early observed in Duchenne muscular dystrophy (Bulfield *et al.*, 1984), leading to progressive muscle fiber weakness and death (Burr and Molkentin, 2015). Incidentally, our swim tunnel experiments showed that the muscle performance was significantly reduced in mutant fish, indicating that the BM mutation does induce muscle weakness as observed in the human disease, likely caused by a pathogenic elevated SR Ca^{2+} efflux.
Although the t-tubule structure is not altered in mutant fish, our DHPR immunolabeling data indicate that the mean distance between fluorescent foci, corresponding to locations of DHPRs clusters facing RyR_1s at the level of triads, is very significantly shorter in mutant fish. This points out mis-localization of DHPRs resulting from Col6 deficiency in mutant fish that could explain the observed dysfunction of DHPR. Additionally, DHPR proteins are anchored in the membrane of t-tubules that penetrate radially the muscle fiber surrounding myofibrils, so that fluorescent DHPR foci detected with confocal microscopy correspond to DHPR clusters distributed in the same transversal plane separated by distance coinciding with the 1-2 µm range of diameter of myofibrils. Consequently, it could be also envisioned that the shorter distance between foci results from reduced diameters of myofibrils in mutant fish. Such a reduced diameter of myofibrils may be issued from a muscle degenerative process that could further explain the observed reduced force output. Along the same line, adult *col6a1* null fish were found to display defective muscle organization and impaired swimming capabilities (Toneletto et al., 2022).
ColVI has been shown to interact with a number of molecules in the extracellular matrix, but the molecular link allowing Col6 deficiency to be transduced into muscle fiber dysfunction remained so far elusive (Cescon et al., 2015). Our study gives evidence that this link, which should necessarily be trans-membranous, is the DHPR. In contrast to cardiac cell t-tubules, in which ColVI has been found to be located (Crossman et al., 2017), we did not observe ColVI immunoreactivity within the skeletal muscle t-tubules neither of whole mount zebrafish larvae nor of frozen sections of juvenile and adult fish. The diameter of skeletal muscle t-tubule is theoretically large enough for one ColVI filament (6 to 10 nm) to fit into the t-tubule lumen (20 to 40 nm). However, ColVI is generally associated to the muscle basement membrane in skeletal muscles which is about 70 nm thick, 140 nm if we consider that the sarcolemma is invaginated with its basement membrane to form the t-tubules. Additionally, ColVI being produced by fibroblasts in skeletal muscle, it is very unlikely that the ColVI tetramers diffuse to the t-tubules to form filaments that is the last step of ColVI biosynthesis. A direct interaction between ColVI and DHPR is thus very unlikely. But, as proposed by Zanotti et al. (2023), we suggest that Col6 deficiency in BM leads to instability in the basal lamina and weakening of the extracellular matrix mechanical support to muscle membrane. It can be hypothesized that instability of basal lamina, possibly amplified by cycles of contraction and relaxation and specifically at the level of the t-tubules where it overhangs openings (Gattazzo et al., 2014), disrupts expression and function of DHPRs anchored in the t-tubule membrane.

In conclusion, by using a unique zebrafish model of BM, our work led to unravel the DHPR as the molecular link transducing Col6 deficiency into alteration of intracellular Ca^{2+} handling and the resulting muscle degenerative process. This study should open new avenues for the treatment of BM using therapeutics targeting the DHPR.

Materials and methods

Zebrafish maintenance and ethics statement

Zebrafish (AB/TU) maintenance and embryo collection were performed at the zebrafish PRECI facility (Plateau de Recherche Expérimentale de Criblage In vivo; UMS CNRS 3444 Lyon Biosciences, Gerland) in compliance with French government guidelines. Embryos obtained from natural spawning were raised following standard conditions. All animal manipulations were performed in agreement with EU Directive 2010/63/EU. The creation and characterization of the *col6a1*$^{\Delta ex14-/-}$ line (Bethlem myopathy fish model) was described in (Ravel et al, 2015) and all procedures have been approved by the French ethical committee.

Generation of guinea pig anti-colVI antibodies

The recombinant zebrafish α1(VI) C-terminal polypeptide was obtained and purified as described in (Tonelotto et al, 2019). Purified recombinant α1(VI) C-terminal polypeptide was used for guinea pig immunization, and the obtained antiserum was purified by antigen-affinity chromatography (Covalab, Lyon). The specificity of purified antibodies was determined by ELISA binding assay and immunoblotting and western blot.

Immunostaining

6-month and 1-year old fishes were terminally anesthetized using 0.2% MS-222 (tricaine methanesulfonate, Sigma-Aldrich). For immunostaining of frozen sections, the trunk was dissected with a razor blade and were fixed overnight at 4°C in 4% PFA and incubated in 30% sucrose in PBS. They were then embedded in OCT freezing medium, and snap-frozen in cold isopentane; 30µm cryosections were obtained using a Leica cryostat and stored at -80°C until use. For immunostaining, frozen sections were rehydrated for 5 min in PBS and incubated 30 min in blocking buffer (1% BSA, 3% goat serum in PBS). Primary antibodies were then incubated overnight at 4°C. After washes in PBS, secondary antibodies, and Rhodamine phalloidin when indicated, were incubated for 1 h at room temperature. After a rapid wash in PBS, nuclei were stained for 5 min with 1.5 µg/mL Hoechst 33258 (Sigma). Samples were washed and mounted in DAKO mounting medium and stored at 4°C until imaging. Primary and secondary antibodies and Rhodamin phalloidin were used at stated dilutions in blocking buffer: guinea-pig anti-colVIα1 antibodies (1:2000); rabbit anti-laminin antibody (1:500; Sigma); goat anti-guinea pig or anti-rabbit IgG coupled to AlexaFluor-488 or AlexaFluor-546 (1:500; Invitrogen); and phalloidin-647 (1:80; Sigma). For immunostaining of isolation of muscle fibers, trunk muscle of the dorso-caudal region of 1-y-old fish were dissected in Tyrode solution and then fixed in were fixed overnight at 4°C in 4% PFA and processed to immunostaining as described above. Samples were observed with a Zeiss LSM 780 spectral confocal microscope (Zeiss, Oberkochen, Germany).

Protein extraction and western blot analysis

One year fish were sacrificed as indicated above and yolks and head were discarded and the skin was peeled off. Samples were snap frozen and store at -8O°C before used. Total extracts were obtained by incubated the samples in 50 mM Tris-HCl (pH 6.8), 5% glycerol, 1% SDS, 4M urea, 50 mM DTT and 0.1% bromophenol blue. Samples were placed on ice and homogenized with a mortar and pestle followed by repeated syringe aspiration. After centrifugation, discard the pellet and heat the supernatant at 95°C for 3 mins. 20 µg of the total protein extracts were separated by SDS-PAGE and transferred to PVDF membrane. Membrane were incubated with our guinea pig antibodies against ColVI and rabbit monoclonal anti-GAPDH (14C10) (1:10,000) as a protein loading control. Immunological detection was

performed with HRP-conjugated secondary antibodies using Immun-Star WesternC as a substrate (Bio-Rad).

Isolation and preparation of zebrafish skeletal muscle fibers

Male 10-13-month-old zebrafish were euthanized with 0.3g/L tricaine (MS222, Sigma), decapitated, and skin was removed. Dorsal trunk muscle of around 3 mm width located just under the dorsal fin was removed and incubated for 40 minutes at 37°C in the presence of Tyrode solution containing 2 mg/mL of collagenase (Sigma, type 1). Single intact muscle fibers were then released by gentle mechanical trituration of the enzyme-treated muscles in a glass-bottomed experimental chamber, in the presence of a culture medium containing 2 % Matrigel (Sigma). A previous study indicated that muscle fibers isolated with this procedure were fast type (Idoux et al., 2022).

T-tubules membrane labelling

For imaging the t-tubule network, isolated zebrafish muscle fibers were incubated for 1h in the presence of 10 µm di-8-anepps in Tyrode solution. Di-8-anepps fluorescence was measured with 488 nm excitation and collected above 505 nm using a confocal microscope equipped with a x63 oil immersion objective and a Zeiss LSM Exciter. To estimate T tubule density and sarcomere length, fluorescence di-8-anepps intensity was reported from 2 distinct locations in the fiber, each comprising a minimum of 60 µm-length and the total width excluding the plasma membrane. The distance between 2 fluorescent peaks was determined from the longitudinal fluorescence profile of a region of interest. The t-tubule density analysis was carried out using an automatic threshold based on Otsu method which produces a binary image of the t-tubules network. The t-tubule density was determined as the ratio of the t-tubule area to the total area selected for the analysis.

Electrophysiology

Prior to trituration, the bottom of the experimental chamber was covered with a thin layer of silicone grease. This enabled single fibers from zebrafish to be covered with additional silicone so that a 50-100 µm-long portion of the fiber extremity was left out, as previously described (Idoux et al., 2020). The culture medium solution was replaced by the extracellular solutions (see Solutions). The tip of a glass micropipette filled with an intracellular-like solution containing a Ca^{2+}-sensitive dye (see intracellular Ca^{2+} measurements) was inserted into the silicone-embedded fiber portion. The silver-chloride wire inside the micropipette was connected to an RK-400 patch-clamp amplifier (Bio-Logic, Claix, France) used in whole-cell voltage-clamp or current-clamp configuration. Command voltage or current pulse generation was achieved with an analog-digital converter (Digidata 1322A, Axon Instruments, Foster City, CA) controlled by pClamp 9 software (Axon Instruments). The tip of the micropipette was gently crushed against the bottom of the chamber to reduce the series resistance and to allow internal dialysis of the fiber. Current and voltage changes were acquired at a sampling frequency of 10 and 50 kHz respectively. All experiments were performed at room temperature (20–22°C).

Charge movement currents were calculated using conventional procedures consisting of subtracting scaled control current recorded in response to a 10-mV hyperpolarizing pulse from the current elicited by test depolarizing pulses of identical duration and of various amplitudes from a holding potential of -80 mV. Charge movement was quantified by integrating the transient outward current after the onset of the test pulse (Q_{on}) and subsequently normalized to cell capacitance (nC/µF).

Intracellular Ca^{2+} measurements

- *Intracellular Ca^{2+} measurements in response to voltage changes*

Prior to voltage clamp, the indo-1 dye, diluted at a concentration of 0.2 mM in an intracellular-like solution (see solutions), was dialyzed into the fiber cytoplasm through the microelectrode inserted through the silicone, within the insulated part of the fiber. Intracellular equilibration of the solution was allowed for a period of 20 min before initiating measurements. Indo-1 fluorescence was measured on an inverted Nikon Diaphot epifluorescence microscope equipped with a commercial optical system,

allowing the simultaneous detection of fluorescence at 405 nm (F405) and 485 nm (F485) by two photomultipliers (IonOptix, Milton, MA, USA) upon 360 nm excitation. Background fluorescence at both emission wavelengths was measured next to each fiber tested and was then subtracted from all measurements. Fluorescence signals were acquired at a sampling frequency of 50 kHz. The standard ratio method was used with the parameters: R=F405/F485, R_{min}, R_{max}, Kd and β having their usual definitions. Results were expressed in terms of indo-1 % saturation. In cells values for R_{min}, R_{max} and β used were 0.3, 1.61 and 2, respectively. Kd was assumed to be 350 nM. No correction was made for indo-1–Ca^{2+} binding and dissociation kinetics. The displayed Ca^{2+} signal traces were smoothed using adjacent averaging of a number of datapoints specified in figure legends.

- Intracellular Ca^{2+} measurements around resting potentials

The non-ratiometric Fluo-4 dye, diluted at a concentration of 0.1 mM in an intracellular-like solution (See solutions), was dialyzed into the fiber cytoplasm through the microelectrode during 20 min before initiating recordings. Fluo-4 fluorescence was measured with 488 nm excitation and collected above 505 nm on a confocal imaging microscope conducted with a Zeiss LSM Exciter and equipped with a x63 oil immersion objective. Cytosolic Ca^{2+} was recording by measuring the changes of Fluo-4 fluorescence elicited by 25 consecutive confocal frames every 500 ms during long voltage clamp depolarizing pulses of increasing amplitude from a holding potential of -90 mV. Fluo-4 Ca^{2+} transients were expressed as F/F_0, where F_0 is the basal fluorescence measured at -90 mV.

- Measurement of Ca^{2+} sparks

Isolated muscle fibres were incubated for 30 min in the presence of 10 µmol/L Fluo-4 acetoxymethyl ester (AM). After 4 times washing with Tyrode solution, 40 consecutive confocal frames of fluo-4 fluorescence were acquired in each fiber at 1 Hz frequency. To quantify the Ca^{2+} sparks activity, images in the stack were smoothed and the standard deviation of fluorescence intensity at each pixel position, along the stack, was calculated. The 10% largest values in the standard deviation image were removed to calculate the mean standard deviation of silent areas. The active area was then defined as pixel positions exhibiting at least 1.5 × larger values of standard deviation than the mean standard deviation value from silent areas. This active area was expressed as percentage of total analyzed area.

Measurement of trunk muscle force

Procedures and measurements were performed as previously reported (Malbouyres et al., 2022)). Two wpf fish were briefly placed in a beaker containing 0.168 mg/mL of tricain (3-amino benzoic acidethylester, Sigma-Aldrich, A5040). The head was crushed and fish were transferred to a Tyrode solution. Under binocular control, fish head and tail extremities were glued with surgical glue (Histoacryl, B Braun) on homemade thin aluminum foils pierced with a small hole allowing to attach the head portion of the fish to the arm of an AE801 force transducer and the tail portion to a fixed pin. Fish were stimulated by field electrodes placed on either side of the fish using a Harvard apparatus 6002 stimulator. In each fish, the voltage of 0.5 ms duration pulses was increased to give maximal twitch response and the voltage used for measuring maximal force was set at 20% above this maximal value. The fish was then gradually stretched on the side of the transducer moved with a micromanipulator until maximal twitch force was obtained. The force signal was recorded at 10 kHz sampling frequency using the WinWCP software (Strathclyde University, UK) driving an AD converter (National Instruments, USA).

Measurement of swimming performance

Swimming performance have been measured using a swim tunnel (Loligo Systems, Denmark). The tunnel is composed of a swimming chamber, where the fish to be tested is placed, a motor fitted with three-bladed propeller to control water flow and a honeycomb placed at each side of the swimming chamber to laminarize the water flow. Before being placed into the swim tunnel, fish were starved 24 hours. Then, the fish was submitted to a short acclimation swimming period (0.5 body length (BL). s^{-1}) prior to starting the swimming challenge. The challenge consists to an increase of the water flow by stage of 1.5 BL. s^{-1} every 15 min. Between each stage, water was refreshed during 3 min. The experiment stopped when the fish did not manage to swim against the current. Then, water flow was

reduced to initial value to permit fish to recover. Fish were then removed from the swim tunnel and anaesthetized using tricaine to determine the total length, mass and sex of each individual. Swimming performance was calculated as critical swimming speed (U_{crit}) according to the formula: $U_{crit} = Ut + t_1.t^{-1}.U_1$, where Ut (in $BL.s^{-1}$) is the highest velocity maintained for an entire step, t_1 (in min) is the time spent until the exhaustion of fish at the last step, t (in min) is the swimming period for each step (i.e. 15 min in the present study) and U_1 is the increment velocity (1.5 $BL.s^{-1}$) (Lucas et al., 2016).

Solutions

The dialyzed intracellular solution contained (in mM): 140 K-glutamate, 5 Na_2-ATP, 5 Na_2 phosphocreatine, 5.5 $MgCl_2$, 5 glucose and 5 Hepes adjusted to pH 7.2 with KOH, except for the experiments devoted to the measurement of intramembrane charge movements (Fig. 2), for which the dialyzed intracellular solution contained (in mM): 140 Cs-aspartate, 5 Mg-ATP, 1 $MgCl_2$, 10 EGTA-CsOH and 5 Hepes. The Tyrode solution used in current-clamp conditions contained (in mm): 140 NaCl, 5 KCl, 2.5 $CaCl_2$, 2 $MgCl_2$ and 10 Hepes, adjusted to pH 7.2 with NaOH. The extracellular solution used for measurements of charge movements and Ca^{2+} signals in voltage-clamp conditions contained (in mm): 140 TEAmethanesulphonate, 2.5 $CaCl_2$, 2 $MgCl_2$, 1 4AP, 0.002 TTX and 10 Hepes, adjusted to pH 7.2. N-benzyl-p-toluene sulphonamide was added in extracellular solutions at 50 µM.

Statistical analysis

Statistical analysis was performed using Microcal Origin and GraphPad Prism. Least-squares fits were performed using a Marquardt–Levenberg algorithm routine included in Microcal Origin. Data are given as means ± S.E.M. For experiments performed on isolated muscle fibers, normality of data distribution was assessed using Shapiro-Wilk test and statistical differences were determined using a nested t-test taking into account the number of fibers from each animal (Fig. 2, 4, 5, 6, 7 and 8). For data not normally distributed, statistical differences were determined using unpaired Mann Whitney Wilcoxon test (Fig. 3 and 8). Numbers of individual measurements and individual animals used are mentioned in the figure legends. Differences were considered significant when $P < 0.05$. Labels *, ** and *** indicate $P < 0.05$, $P < 0.005$ and $P < 0.0005$ respectively.

References

Allard, B. 2018. From excitation to intracellular Ca^{2+} movements in skeletal muscle: Basic aspects and related clinical disorders. *Neuromuscul Disord* 28, 394-401.

Bellinger, A.M., S. Reiken, C. Carlson, M. Mongillo, X. Liu, L. Rothman, S. Matecki, A. Lacampagne, and A.R. Marks. 2009. Hypernitrosylated ryanodine receptor/calcium release channels are leaky in dystrophic muscle. *Nat Med* 15:325–330.

Bonaldo, P. 1998. Collagen VI deficiency induces early onset myopathy in the mouse: an animal model for Bethlem myopathy. *Hum Mol Genet* 7:2135–2140.

Bönnemann, C.G. 2011. The collagen VI-related myopathies: muscle meets its matrix. *Nat Rev Neurol* 7:379–390.

Bulfield, G., Siller W.G., Wight P.A., and Moore, K.J. 1984. X chromosome-linked muscular dystrophy (mdx) in the mouse. *Proc Natl Acad Sci USA* 81:1189–1192.

Burr, A.R., and J.D. Molkentin. 2015. Genetic evidence in the mouse solidifies the calcium hypothesis of myofiber death in muscular dystrophy. *Cell Death Differ* 22:1402–1412.

Cescon, M., F. Gattazzo, P. Chen, and P. Bonaldo. 2015. Collagen VI at a glance. *J Cell Sci* 128:3525-3531.

Cescon, M., I. Gregorio, N. Eiber, D. Borgia, A. Fusto, P. Sabatelli, M. Scorzeto, A. Megighian, E. Pegoraro, S. Hashemolhosseini, and P. Bonaldo. 2018. Collagen VI is required for the structural and functional integrity of the neuromuscular junction. *Acta Neuropathol* 136:483–499.

Colombatti, A., M.T. Mucignat, and P. Bonaldo. 1995. Secretion and matrix assembly of recombinant type VI collagen. *J Biol Chem* 270:13105–13111.

Crossman DJ, Shen X, Jüllig M, Munro M, Hou Y, Middleditch M, Shrestha D, Li A, Lal S, Dos Remedios CG, Baddeley D, Ruygrok PN, Soeller C. 2017. Increased collagen within the transverse tubules in human heart failure. *Cardiovasc Res* 113:879-891.

Franzini-Armstrong C, Landmesser L, Pilar G. 1975. Size and shape of transverse tubule openings in frog twitch muscle fibers. *J Cell Biol* 64:493–497.

Gattazzo F, Urciuolo A, Bonaldo P. 2014. Extracellular matrix: A dynamic microenvironment for stem cell niche. *Biochim Biophys Acta* 1840:2506-2519.

Idoux, R., S. Bretaud, C. Berthier, F. Ruggiero, V. Jacquemond, and B. Allard. 2022. Superfast excitation-contraction coupling in adult zebrafish skeletal muscle fibers. *J Gen Physiol* 154:e202213158.

Idoux, R., C. Fuster, V. Jacquemond, A. Dayal, M. Grabner, P. Charnet, and B. Allard. 2020. Divalent cations permeation in a Ca^{2+} non-conducting skeletal muscle dihydropyridine receptor mouse model. *Cell Calcium* 91:102256.

Irwin, W.A., N. Bergamin, P. Sabatelli, C. Reggiani, A. Megighian, L. Merlini, P. Braghetta, M. Columbaro, D. Volpin, G.M. Bressan, P. Bernardi, and P. Bonaldo. 2003. Mitochondrial dysfunction and apoptosis in myopathic mice with collagen VI deficiency. *Nat Genet* 35:367–371.

Lamandé, S.R., and J.F. Bateman. 2018. Collagen VI disorders: Insights on form and function in the extracellular matrix and beyond. *Matrix Biol* 71–72:348–367.

Lampe, A.K. 2005. Collagen VI related muscle disorders. *J Med Genet* 42:673–685.

Lucas, J., I. Percelay, T. Larcher, and C. Lefrançois. 2016. Effects of pyrolytic and petrogenic polycyclic aromatic hydrocarbons on swimming and metabolic performance of zebrafish contaminated by ingestion. *Ecotoxicol Environ Saf* 132:145–152.

Malbouyres M, Guiraud A, Lefrançois C, Salamito M, Nauroy P, Bernard L, Sohm F, Allard B, Ruggiero F. 2022. Lack of the myotendinous junction marker col22a1 results in posture and locomotion disabilities in zebrafish. *Matrix Biol* 109:1-18.

Perni, S., K.C. Marsden, M. Escobar, S. Hollingworth, S.M. Baylor, and C. Franzini-Armstrong. 2015. Structural and functional properties of ryanodine receptor type 3 in zebrafish tail muscle. *J Gen Physiol* 145:173–184.

Radev, Z., J.-M. Hermel, Y. Elipot, S. Bretaud, S. Arnould, P. Duchateau, F. Ruggiero, J.-S. Joly, and F. Sohm. 2015. A TALEN-Exon Skipping Design for a Bethlem Myopathy Model in Zebrafish. *PLoS ONE* 10:e0133986.

Ríos, E. 2018. Calcium-induced release of calcium in muscle: 50 years of work and the emerging consensus. *J Gen Physiol* 150:521–537.

Robin, G., and B. Allard. 2012. Dihydropyridine receptors actively control gating of ryanodine receptors in resting mouse skeletal muscle fibres. *J Physiol* 590:6027–6036.

Robin, G., C. Berthier, and B. Allard. 2012. Sarcoplasmic reticulum Ca2+ permeation explored from the lumen side in mdx muscle fibers under voltage control. *J Gen Physiol* 139:209–218.

Shirokova, N., J. García, and E. Ríos. 1998. Local calcium release in mammalian skeletal muscle. *J Physiol* 512:377–384.

Telfer, W.R., A.S. Busta, C.G. Bonnemann, E.L. Feldman, and J.J. Dowling. 2010. Zebrafish models of collagen VI-related myopathies. *Hum Mol Genet* 19:2433–2444.

Tonelotto V, Consorti C, Facchinello N, Trapani V, Sabatelli P, Giraudo C, Spizzotin M, Cescon M, Bertolucci C, Bonaldo P. 2022. Collagen VI ablation in zebrafish causes neuromuscular defects during developmental and adult stages. *Matrix Biol* 112:39-61.

Walker SM, Schrodt GR. 1965. Continuity of the t-system with the sarcolemma in rat skeletal muscle fibers. *J Cell Biol* 27:671–677.

Zanotti S, Magri F, Salani S, Napoli L, Ripolone M, Ronchi D, Fortunato F, Ciscato P, Velardo D, D'Angelo MG, Gualandi F, Nigro V, Sciacco M, Corti S, Comi GP, Piga D. 2023. Extracellular matrix disorganization and sarcolemmal alterations in COL6-related myopathy patients with New Variants of COL6 Genes. *Int J Mol Sci* 24:5551.

Acknowledgments

This work was supported by CNRS, Inserm, INRAE, Ecole Normale Supérieure (ENS) de Lyon, Université Lyon 1, Association Française contre les Myopathies (AFM), Agence Nationale de la Recherche (ANR) and Fondation pour la Recherche Médicale (FRM).

Figure legends

Figure 1: **ColVI deposition, basement membrane organization and ColVI intracellular accumulation in *col6a1$^{\Delta ex14}$* mutant.** (A) Confocal images of 6 months and 1 year old zebrafish muscle cross-section (mf, muscle fibers; arrowheads, aggregates; arrow, interruption. (B) Confocal images of 1 year old zebrafish isolated muscle fibers (mf, muscle fibers; fb, fibroblast). (C) Western blotting 3-8% SDS-PAGE with anti-COLVI antibodies on skin extract with DTT.

Figure 2: **T-tubules network in WT and *col6a1$^{\Delta ex14}$* muscle fibers.** (A) Representative x, y fluorescence confocal images of a WT (left) and a *col6a1$^{\Delta ex14}$* (right) isolated muscle fiber stained with di-8-anepps. Scale bar = 20 µm. (B) Average intensity profiles of di-8-anepps fluorescence in a WT (left) and a *col6a1$^{\Delta ex14}$* (right) isolated muscle fiber. (C) Histograms presenting mean distance between two peaks of di-8-anepps fluorescence (upper panel) and mean t-tubule density index (lower panel) in WT and *col6a1$^{\Delta ex14}$* muscle fibers. Data were collected in 10 fibers from 1 WT fish and in 10 fibers from 1 *col6a1$^{\Delta ex14}$* fish.

Figure 3: **Action potentials in WT and col6a1$^{\Delta ex14}$ muscle fibers.** (A) Action potential elicited by injection of a 0.5-ms-long suprathreshold depolarizing current in current clamp condition in a WT (left) and a *col6a1$^{\Delta ex14}$* (right) isolated muscle fibers. (B) Histograms presenting the maximal amplitude, time to peak and time for 20, 50 and 80 % repolarization of action potential after spike in WT and *col6a1$^{\Delta ex14}$* fibers. Data were obtained in 9 fibers from 3 WT fish and 10 fibers from 2 *col6a1$^{\Delta ex14}$* fish.

Figure 4: **Intramembrane charge movements elicited by membrane depolarization in WT and *col6a1$^{\Delta ex14}$* muscle fibers.** (A) Charge movements recorded in response to 20-ms-long depolarizing pulses from a holding potential of -80 mV to the indicated value in a WT (left) and in a *col6a1$^{\Delta ex14}$* (right) isolated muscle fibers. (B) Relationship between the mean density of charge movements and membrane potential in WT and *col6a1$^{\Delta ex14}$* fibers. Mean data points from the 2 curves were fitted using a Boltzmann equation with values for Q_{max}, $V_{0.5}$ and k of 8.8 ± 0.7 nC/µF, -32.5 ± 1.5 mV and 9 ± 0.4 mV in WT fibers respectively, and of 6.3 ± 0.7, -41.4 ± 1.4 and 6.7 ± 0.4 in *col6a1$^{\Delta ex14}$* fibers respectively. (C) Histograms presenting mean values of Q_{max}, $V_{0.5}$ and k in WT and in *col6a1$^{\Delta ex14}$* fibers. Data were obtained in 23 fibers from 4 WT fish and 24 fibers from 3 *col6a1$^{\Delta ex14}$* fish.

Figure 5: **Voltage-activated Ca^{2+} transients in WT and *col6a1$^{\Delta ex14}$* muscle fibers.** (A) Indo-1 percentage saturation traces in response to 50-ms-long depolarizing pulses of increasing amplitude in a WT (left) and a *col6a1$^{\Delta ex14}$* (right) isolated muscle fibers. Traces have been smoothed using adjacent averaging of 20 datapoints. (B) Relationship between the maximal amplitude of indo-1 percentage saturation and the membrane potential in WT and *col6a1$^{\Delta ex14}$* fibers. Mean datapoints from the 2 curves were fitted using a Boltzmann equation with values for maximal indo-1 saturation, $V_{0.5}$ and k of 53.2 ± 2.6 %, -30.6 ± 0.8 mV and 7.2 ± 0.2 mV in WT fibers respectively, and of 55.6 ± 2.4 %, -35.8 ± 0.9 mV and 7.2 ± 0.3 mV in *col6a1$^{\Delta ex14}$* fibers respectively. (C) Histograms presenting mean values of maximal indo-1 % saturation, resting indo-1 % saturation, $V_{0.5}$ and k in WT and *col6a1$^{\Delta ex14}$* fibers. Data were collected in 50 fibers from 7 WT fish and 66 fibers from 8 *col6a1$^{\Delta ex14}$* fish.

Figure 6: **Inactivation of voltage-activated Ca^{2+} transients in WT and *col6a1$^{\Delta ex14}$* muscle fibers.** (A) Indo-1 signals elicited by 50-ms-depolarizing pulses at 0 mV from holding potentials (HP) increasingly depolarized to the indicated voltages in a WT (left) and a *col6a1$^{\Delta ex14}$* (right) isolated muscle fibers. Traces have been smoothed using adjacent averaging of 5 datapoints. (B) Relationship between mean

relative peak of indo-1 percentage saturation in response to depolarizing pulses at 0 mV and holding potentials in WT and *col6a1*$^{\Delta ex14}$ fibers. Mean data points from the 2 curves were fitted using a Boltzmann equation with values for $V_{0.5}$ and k of -67.7 ± 3.4 mV and 8.2 ± 0.7 mV in WT fibers respectively, and of -59.6 ± 2.7 mV and 6.7 ± 0.6 mV in *col6a1*$^{\Delta ex14}$ fibers respectively. (C) Histograms presenting $V_{0.5}$ (mV) and k (mV) in WT and *col6a1*$^{\Delta ex14}$ fibers. Data have been obtained in 12 fibers from 2 WT fish and 16 fibers from 2 *col6a1*$^{\Delta ex14}$ fish.

Figure 7: **Intracellular Ca^{2+} changes evoked by long duration depolarizing pulses of low amplitude in WT and *col6a1*$^{\Delta ex14}$ muscle fibers.** (A) Fluo-4 fluorescence changes expressed as $F/F_{-90\ mV\ BE}$, recorded at a frequency of 2 Hz in response to 10-s-long depolarizing pulses of increasing amplitude from a holding potential of -90 mV in a WT (left) and a *col6a1*$^{\Delta ex14}$ (right) isolated muscle fiber, where F and $F_{-90\ mV\ BE}$ correspond to the maximum fluorescence measured during the pulse and $F_{-90\ mV\ BE}$ to the fluorescence measured at -90 mV at the beginning of the experiment, respectively. (B) Relationship between maximal amplitude of $F/F_{-90\ mV\ BE}$ and membrane potential in WT and *col6a1*$^{\Delta ex14}$ fibers. Data have been obtained in 30 fibers from 5 WT fish and in 34 fibers from 5 *col6a1*$^{\Delta ex14}$ fish. (C) Fluo-4 fluorescence changes expressed as $F_{-90\ mV\ BP}/ F_{-90\ mV\ BE}$, where $F_{-90\ mV\ BP}$ corresponds to the fluorescence measured at -90 mV before the pulse. Data have been obtained in 20 fibers from 4 WT fish and in 28 fibers from 4 *col6a1*$^{\Delta ex14}$ fish.

Figure 8: **Ca^{2+} sparks activity in resting WT and *col6a1*$^{\Delta ex14}$ muscle fibers.** (A) Confocal fluo-4 fluorescence images during a sequence of 40 successive frames in a WT fiber (left) and a *col6a1*$^{\Delta ex14}$ (right) isolated muscle fiber. Arrows point to Ca^{2+} sparks. Scale bar: 10 µm (B) Histogram presenting mean active area (displaying Ca^{2+} sparks) in WT and *col6a1*$^{\Delta ex14}$ groups. (C) Histograms presenting the number of WT and *col6a1*$^{\Delta ex14}$ fibers displaying increasing range of active area. Data have been obtained in 23 fibers from 2 WT fish and in 23 fibers from 2 *col6a1*$^{\Delta ex14}$ fish.

Figure 9: **Muscle contractile force and swimming performance of WT and *col6a1*$^{\Delta ex14}$ fish.** (A) Representative twitch responses elicited by single supramaximal electric shocks of 0.5 ms duration in WT and *col6a1*$^{\Delta ex14}$ fish. (B) Histograms showing mean twitch amplitudes in the two fish lines. (C) Swimming tunnel montage images of a WT and a *col6a1*$^{\Delta ex14}$ fish on water flow of 5 $BL.s^{-1}$. (D) Mean critical swimming speed (U_{crit}) of the two fish lines.

Figure 10: **DHPR distribution along t-tubules in WT and *col6a1*$^{\Delta ex14}$ muscle fibers.** (A) Airyscan detector and processing of fluorescence confocal images of 1 year old zebrafish isolated muscle fibers labelled with antibodies raised against the α1s subunit of DHPR. (B) Distances between immunofluorescent foci (900 length measurements in 4 WT and 4 mutant fish).

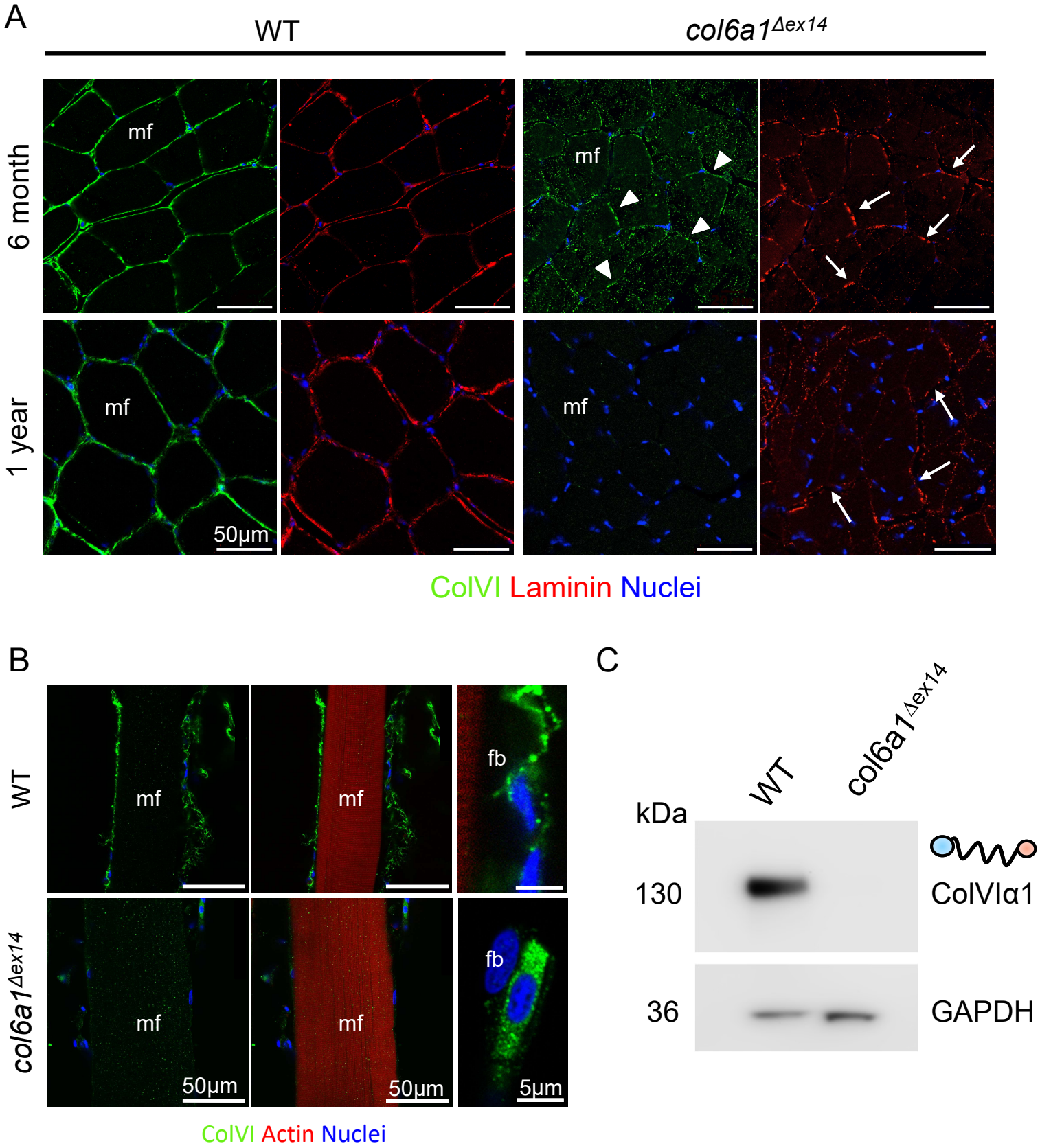
A
WT
col6a1Δex14
6 month
1 year
mf
50µm
ColVI Laminin Nuclei
B
WT
col6a1Δex14
mf
fb
50µm
5µm
ColVI Actin Nuclei
C
WT
col6a1Δex14
kDa
130
36
ColVIα1
GAPDH

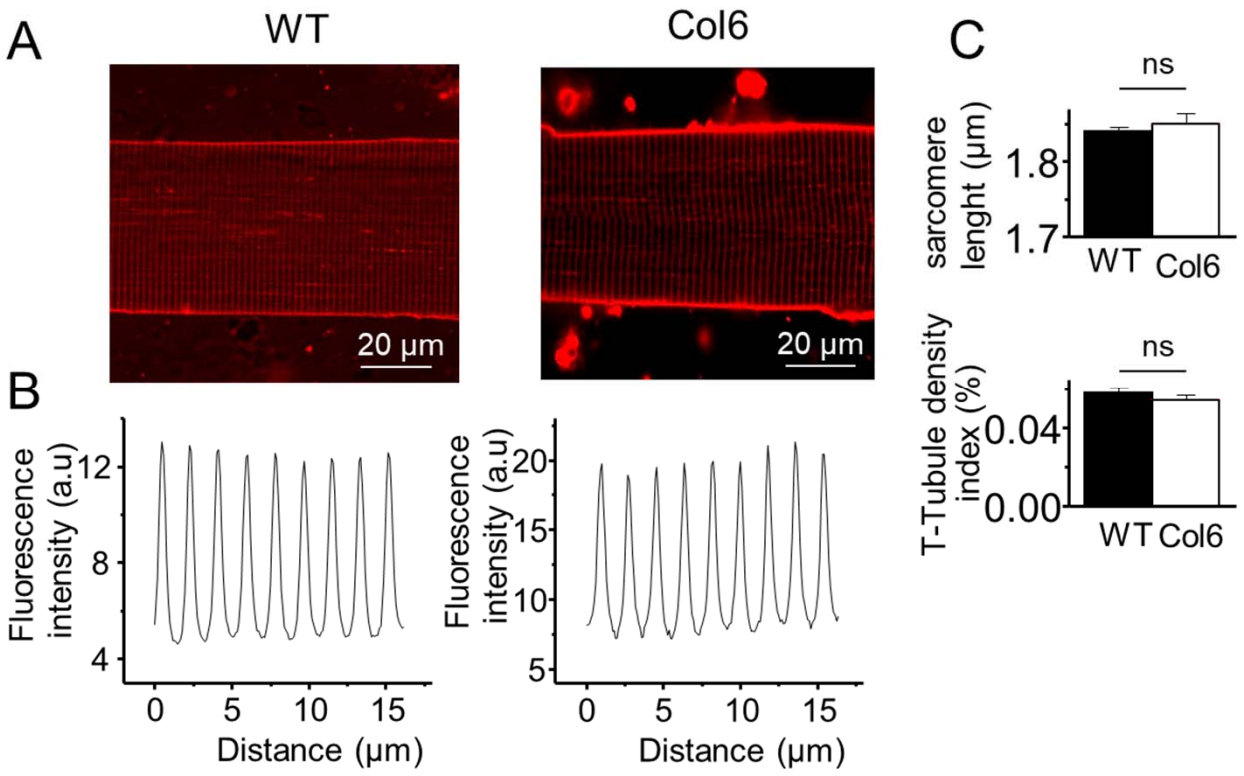
A
WT
Col6
20 µm
20 µm
B
Fluorescence intensity (a.u)
12
8
4
0
5
10
15
Distance (µm)
Fluorescence intensity (a.u)
20
15
10
5
0
5
10
15
Distance (µm)
C
ns
sarcomere lenght (µm)
1.8
1.7
WT
Col6
ns
T-Tubule density index (%)
0.04
0.00
WT
Col6

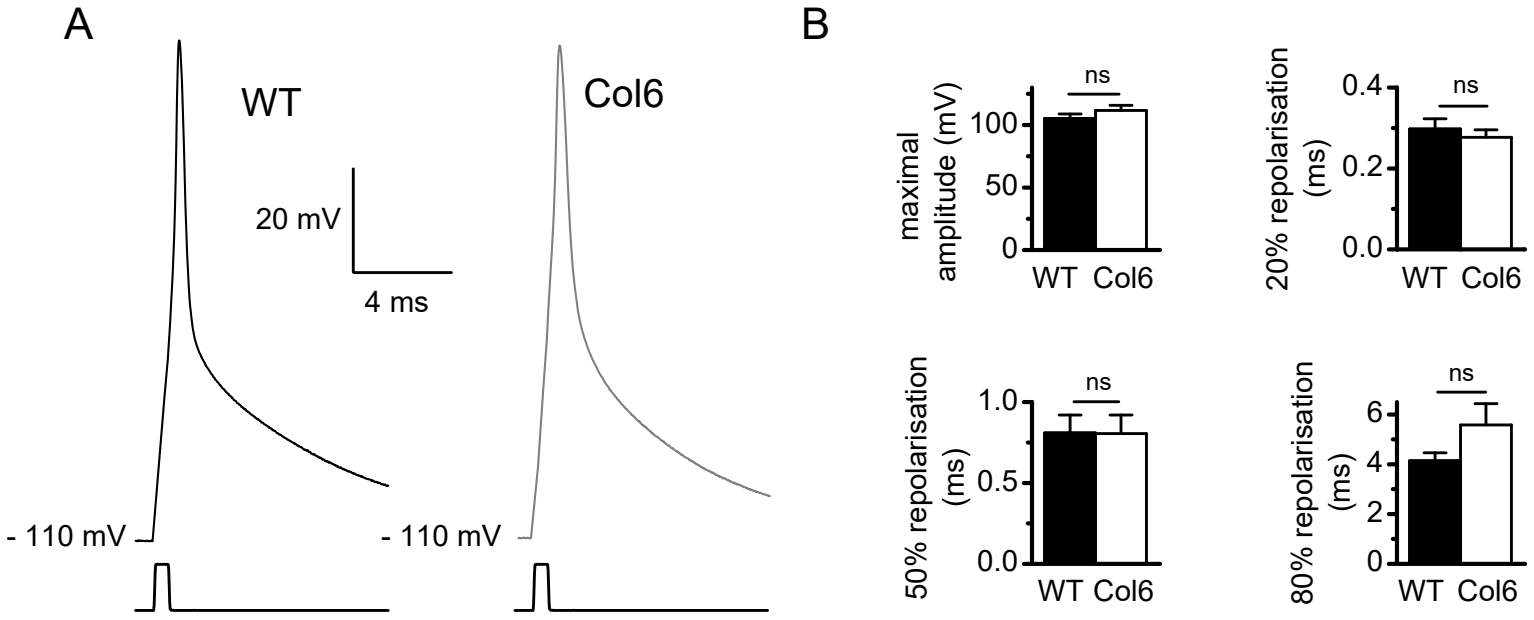
A
WT
Col6
20 mV
4 ms
- 110 mV
- 110 mV
B
maximal amplitude (mV)
100
50
0
ns
WT
Col6
20% repolarisation (ms)
0.4
0.2
0.0
ns
WT
Col6
50% repolarisation (ms)
1.0
0.5
0.0
ns
WT
Col6
80% repolarisation (ms)
6
4
2
0
ns
WT
Col6

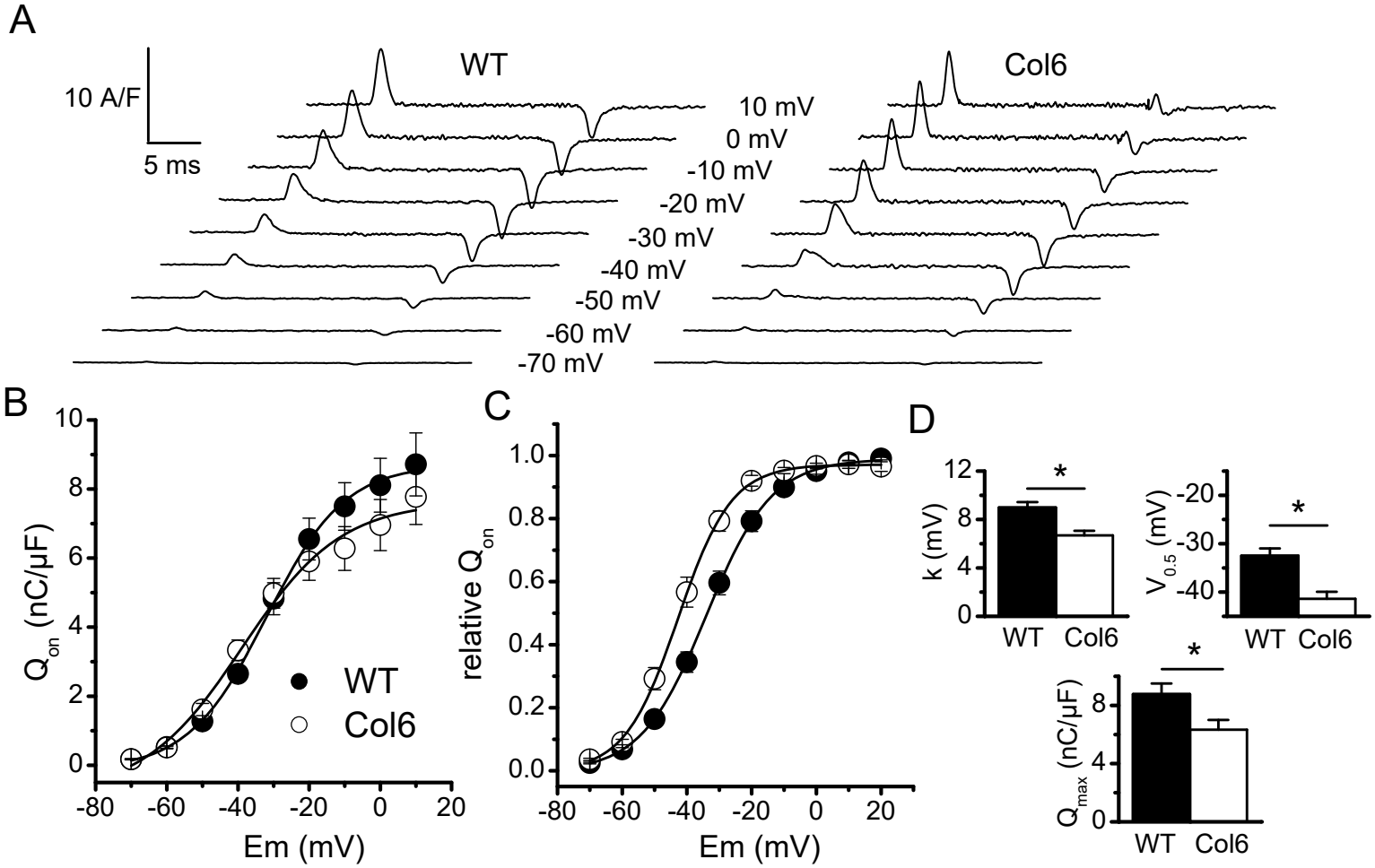
A
WT
Col6
10 A/F
5 ms
10 mV
0 mV
-10 mV
-20 mV
-30 mV
-40 mV
-50 mV
-60 mV
-70 mV
B
Q_{on} (nC/µF)
Em (mV)
WT
Col6
C
relative Q_{on}
Em (mV)
D
k (mV)
$V_{0.5}$ (mV)
Q_{max} (nC/µF)
WT
Col6
*

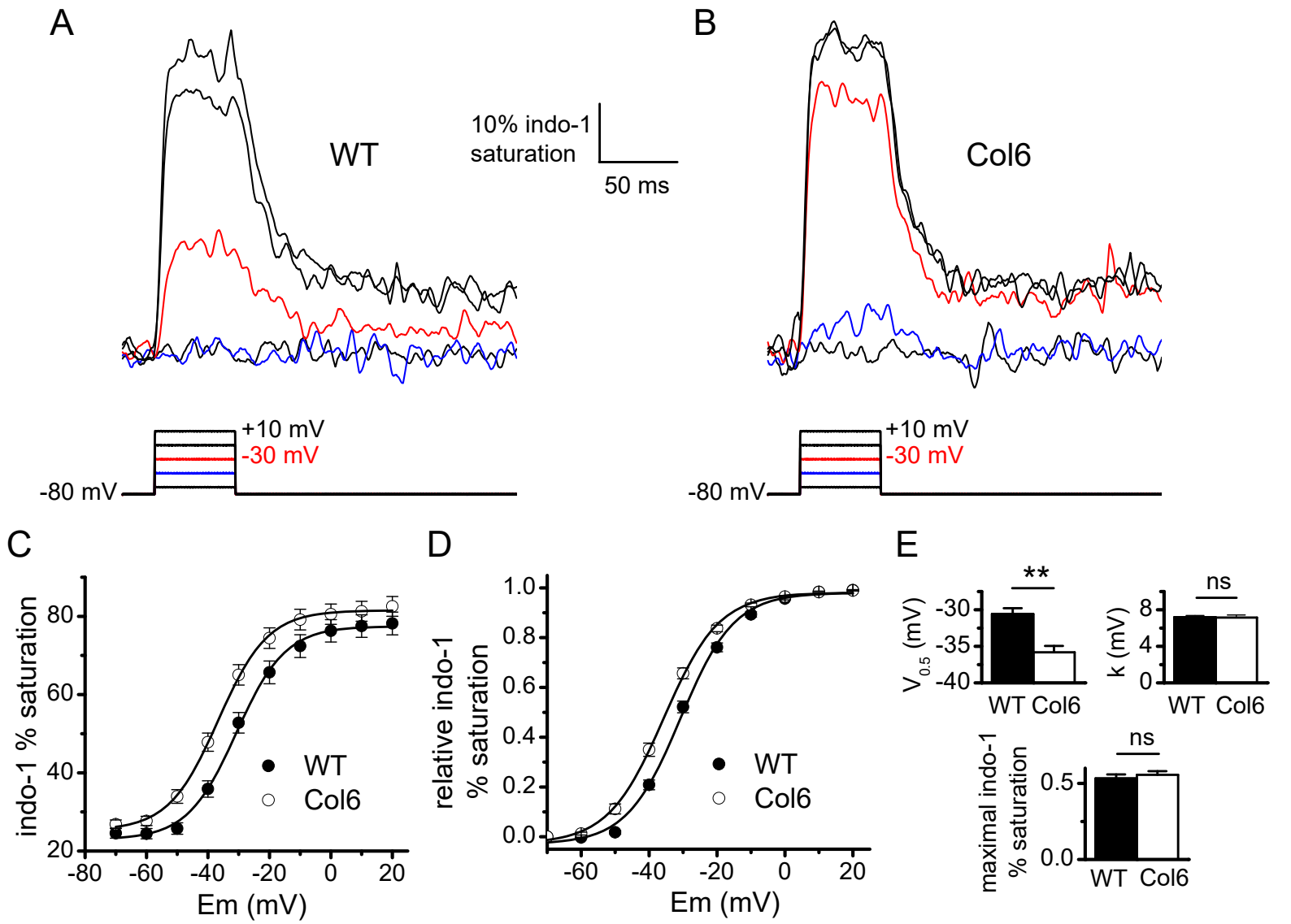
A
WT
10% indo-1
saturation
50 ms
+10 mV
-30 mV
-80 mV
B
Col6
+10 mV
-30 mV
-80 mV
C
indo-1 % saturation
Em (mV)
WT
Col6
D
relative indo-1
% saturation
Em (mV)
WT
Col6
E
**
ns
ns
$V_{0.5}$ (mV)
k (mV)
maximal indo-1
% saturation
WT
Col6

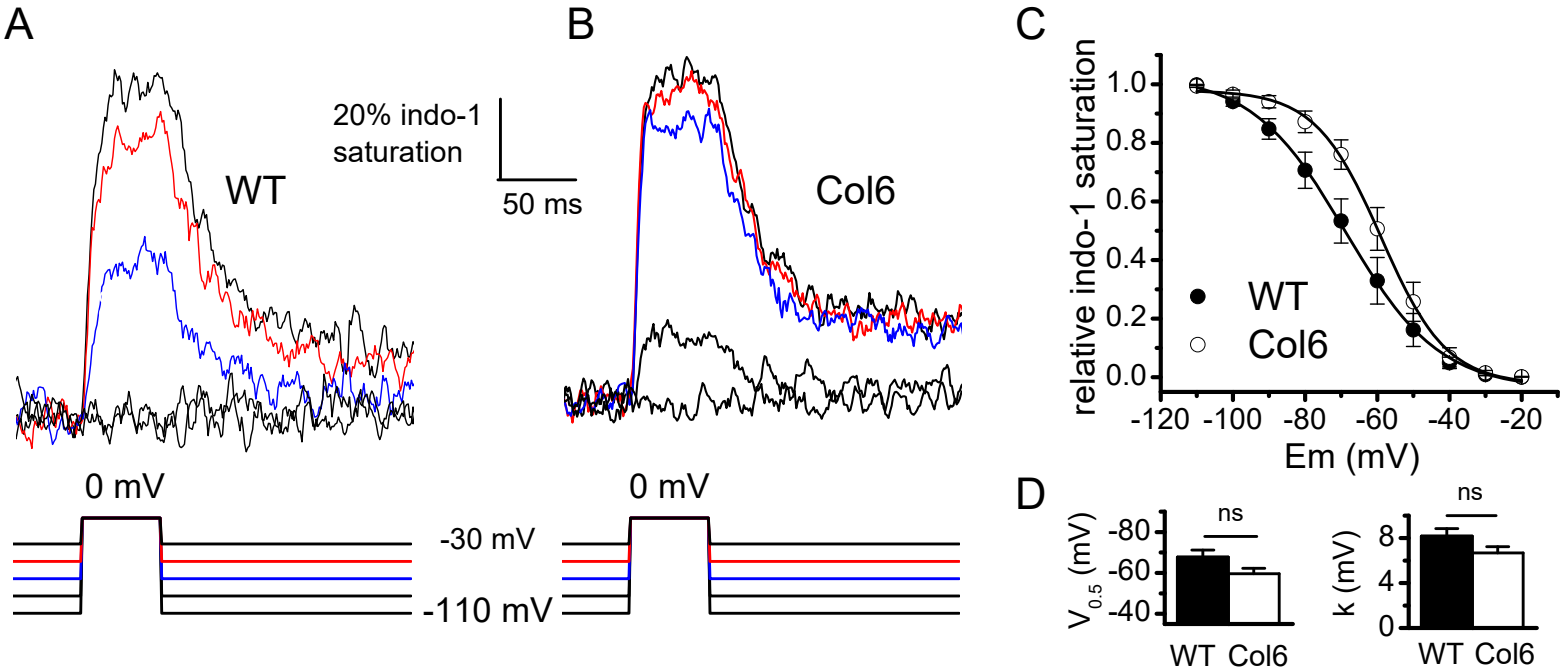
A
B
C
D
20% indo-1
saturation
50 ms
WT
Col6
0 mV
-30 mV
-110 mV
relative indo-1 saturation
1.0
0.8
0.6
0.4
0.2
0.0
-120 -100 -80 -60 -40 -20
Em (mV)
WT
Col6
ns
$V_{0.5}$ (mV)
-80
-60
-40
k (mV)
8
4
0

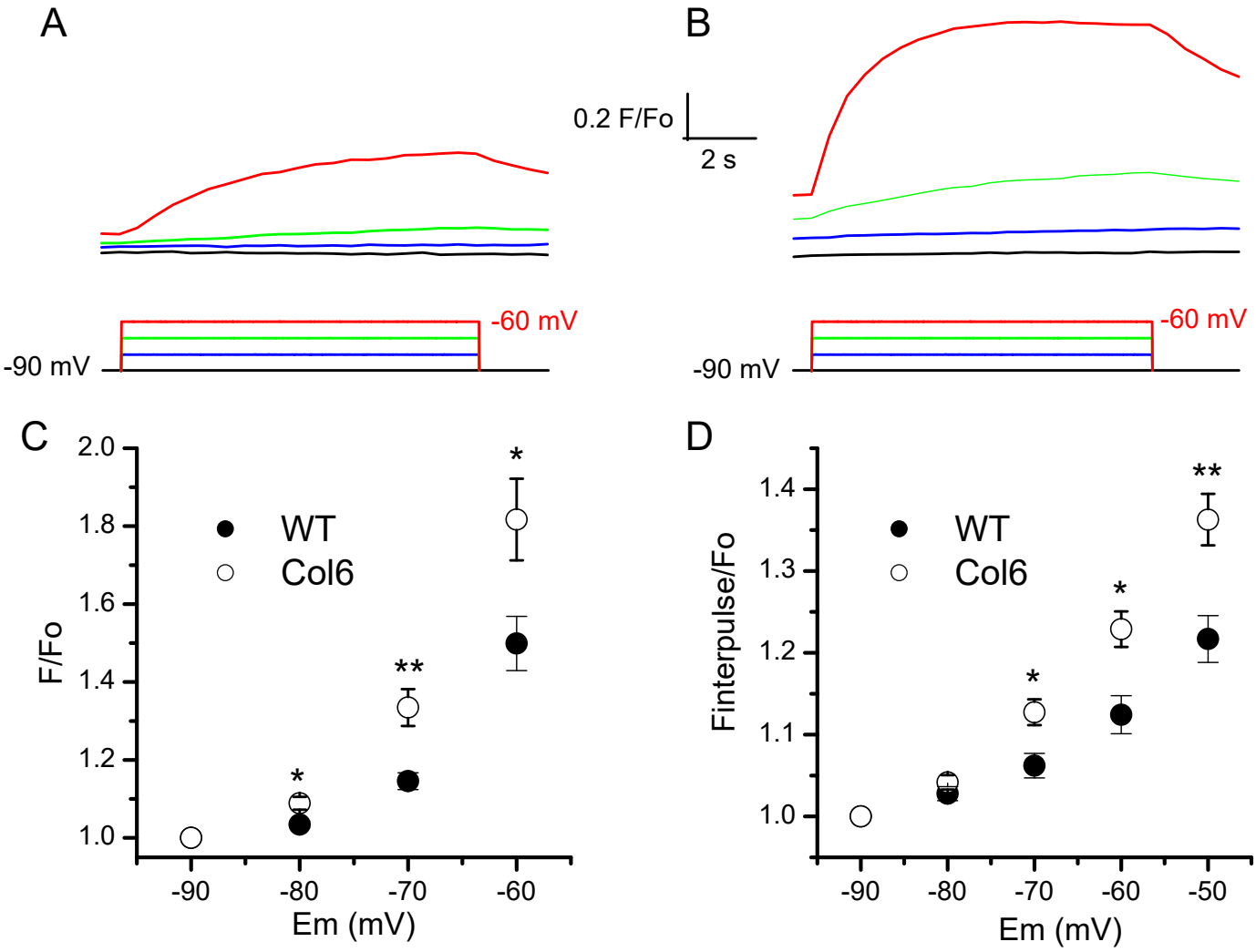
A
B
0.2 F/Fo
2 s
-60 mV
-90 mV
-60 mV
-90 mV
C
D
WT
Col6
F/Fo
Finterpulse/Fo
Em (mV)
Em (mV)
*
**
*
*
**

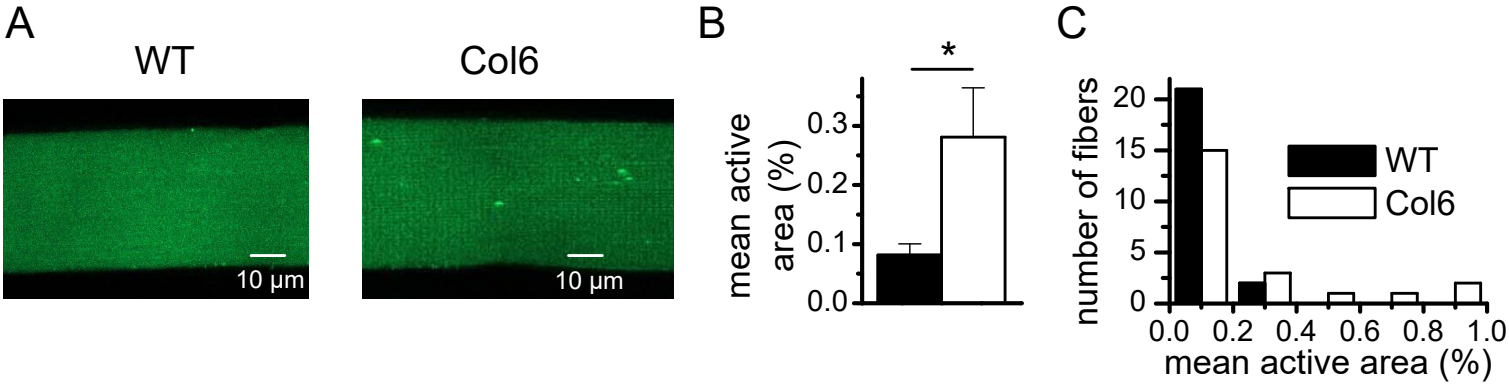
A
WT
Col6
10 µm
10 µm
B
*
mean active area (%)
0.0
0.1
0.2
0.3
C
number of fibers
0
5
10
15
20
WT
Col6
0.0
0.2
0.4
0.6
0.8
1.0
mean active area (%)

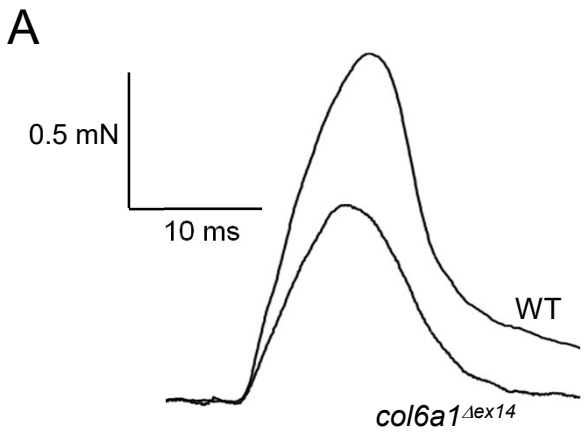
A
0.5 mN
10 ms
WT
col6a1Δex14

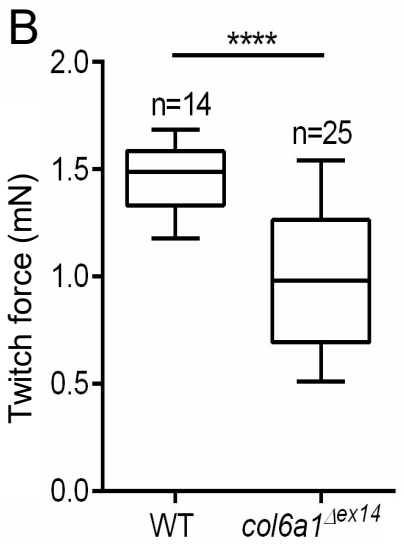
B
****
n=14
n=25
Twitch force (mN)
2.0
1.5
1.0
0.5
0.0
WT
col6a1Δex14

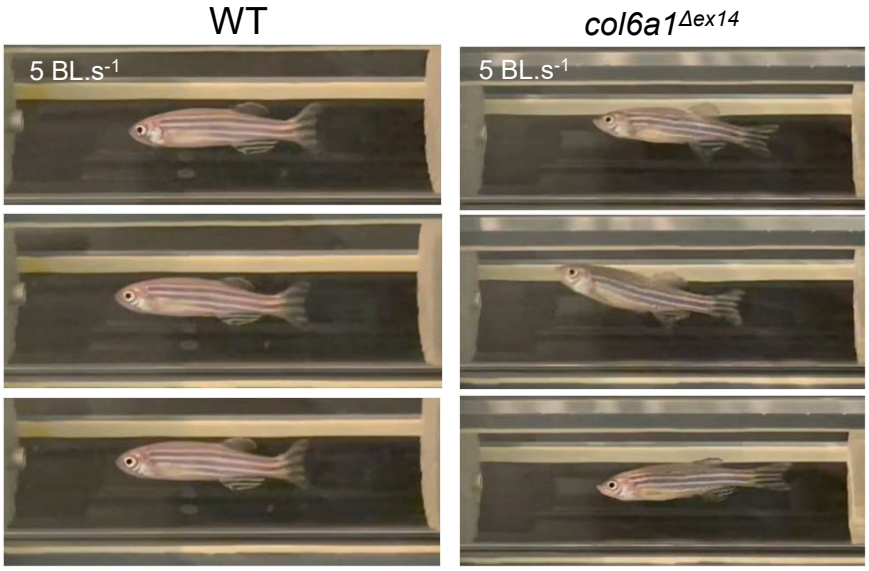
C
WT
col6a1Δex14
5 BL.s-1
5 BL.s-1

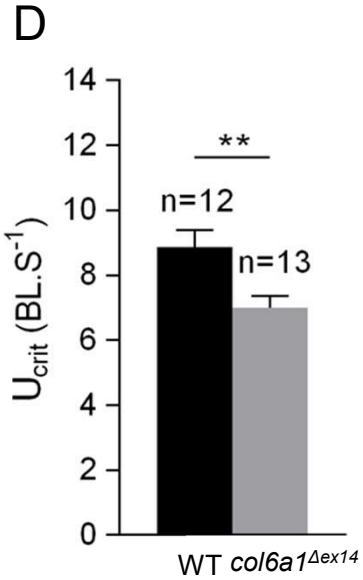
D
**
n=12
n=13
Ucrit (BL.S-1)
14
12
10
8
6
4
2
0
WT
col6a1Δex14

A

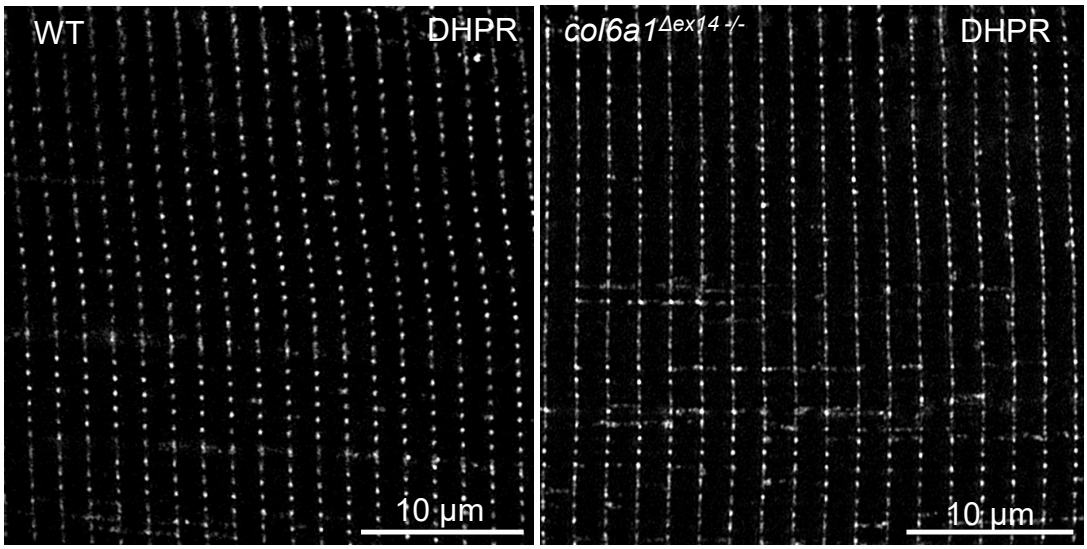
WT
DHPR
10 µm
col6a1Δex14 -/-
DHPR
10 µm

B

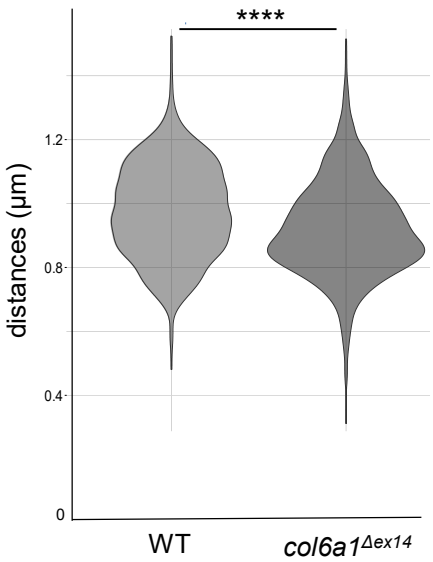
****
distances (µm)
1.2
0.8
0.4
0
WT
col6a1Δex14